RSC Advances

ROYAL SOCIETY OF CHEMISTRY

PAPER

View Article Online
View Journal | View Issue

Cite this: *RSC Adv.*, 2026, **16**, 5194

Hybrid microwave annealing-induced formation of an α-Fe_2O_3/$ZnWO_4$ interface for photoelectrochemical water splitting and study of its charge transport mechanism

K. Ramachandran,[a] A. Nirmala Grace,[b] George Jacob,[b] M. Vijayan,[a] E. Anbarasan[a] and R. Ramesh *[a]

Received 6th October 2025
Accepted 4th January 2026

DOI: 10.1039/d5ra07601c

rsc.li/rsc-advances

The α-Fe_2O_3 photoanode is an efficient semiconductor material for photoelectrochemical (PEC) water oxidation due to its favorable bandgap, chemical stability, and natural abundance. However, the rapid recombination of photoexcited electrons (e^-) and holes (h^+) impedes the PEC efficiency. Herein, an α-Fe_2O_3/$ZnWO_4$ heterojunction photoanode was synthesized by combining hydrothermal and hybrid microwave annealing methods. The α-Fe_2O_3/$ZnWO_4$ heterojunction photoanode demonstrated a photocurrent density of 0.86 mA cm^{-2} at 1.23 V *vs.* RHE, which is more than 2.2 times that of pure $ZnWO_4$ (0.06 mA cm^{-2}) and the α-Fe_2O_3 photoanode (0.29 mA cm^{-2}). In contrast, the α-Fe_2O_3/$ZnWO_4$ photoanode exhibited an improved ABPE value of 0.10% at 1.0 V *vs.* RHE. The significantly improved charge separation efficiency and reduced charge recombination were attributed to hole storage in a $ZnWO_4$ heterojunction layer.

1. Introduction

There is an urgent need to develop clean and sustainable energy technologies due to the severe global environmental pollution caused by the excessive utilization of fossil fuels such as coal and petroleum energy resources.[1,2] Hydrogen is a promising renewable energy source that would adequately supply energy for the entire planet.[3,4] Researchers are interested in hydrogen energy (H_2) through water splitting using a photoelectrochemical (PEC) cell because it is a clean, zero-emission process that is environmentally friendly and low-cost, among many other alternatives and renewable energy sources.[5,6]

In 1972, the TiO_2 semiconductor was first employed by Honda and Fujishima to split water through the PEC system.[7] Additional semiconductor materials such as $BiVO_4$,[8] TiO_2,[9] ZnO,[10] WO_3,[11] and α-Fe_2O_3 (ref. 12) have been investigated for PEC water oxidation. Among them, α-Fe_2O_3 is an especially promising semiconductor candidate for water oxidizing due to its excellent stability and environmental friendliness, low-cost, and suitable band gap ($E_g \approx 2.1$ eV). However, the more practical application of pure α-Fe_2O_3 is limited by several challenges, including low electron mobility, a short hole-diffusion length (2–4 nm), a low light absorption coefficient resulting from its indirect band gap, and short carrier lifetime. Moreover, the conduction band edge position of a pure α-Fe_2O_3 photoanode does not align with the reversible hydrogen potential, necessitating a high over-potential for PEC water reduction. Further, the use of an α-Fe_2O_3 photoanode is more challenging for efficient water oxidation due to its low PEC water oxidation kinetics and inefficient charge separation.

Several approaches have been employed to address the challenges associated with using α-Fe_2O_3 for PEC water splitting, such as doping,[13] nanostructuring photoanodes,[14] and the formation of heterojunction photoanodes.[15] During the water oxidation reaction, the charge separation of electrode surfaces is promoted by nanostructuring of the α-Fe_2O_3 photoanode. Various nanostructured forms of α-Fe_2O_3 have been reported with surface morphologies of nanorods,[16] nanotubes,[17] nanosheets,[18] and nanoflowers.[19] One effective method that has been widely used to reduce charge recombination, improve photon absorption, and improve charge separation of α-Fe_2O_3 for effective PEC water splitting is the development of heterojunction structures.

For example, Alotaibi *et al.* reported an α-Fe_2O_3/TiO_2 heterojunction photoanode created by a chemical vapour deposition method that significantly enhanced PEC water splitting performance.[20] The photocurrent density of WO_3 increases by more than a factor of nine upon coupling with α-Fe_2O_3, as reported by Mao *et al.*[21] In addition, Xia *et al.* demonstrated that α-Fe_2O_3/$BiVO_4$ heterojunction photoanodes greatly enhanced PEC performance.[22] Another promising

---

[a] *Department of Physics, Periyar University, Salem-636 011, Tamil Nadu, India. E-mail: rameshphys@gmail.com*

[b] *Centre for Nanotechnology Research (CNR), Vellore Institute of Technology (VIT), Vellore, Tamil Nadu, 632014, India*

approach for improvement of charge separation is the formation of *n–n* type heterostructures, which can facilitate more optimal charge transport properties and separation as well as limit electron/hole (e^-/h^+) recombination. Recently, *n–n* type heterostructures such as CdS/FST,[23] $BiVO_4$/CdS,[24] WO_3/Fe_2O_3,[25] and $WO_3/ZnWO_4$ have been used for PEC water splitting.[26]

Among the various *n–n* type heterostructure semiconductors, $ZnWO_4$ has emerged as an attractive second semiconductor due to its suitable conduction band position, satisfactory electron mobility, and excellent chemical stability. In particular, because of its high stability in acidic and alkaline media, along with strong interfacial superior compatibility with oxide semiconductors, $ZnWO_4$ is highly suitable for constructing heterojunction photoanodes.[27,28] For example, the formation of a $WO_3/ZnWO_4$ heterojunction photoanode is effective for increasing the visible light absorption and charge separation efficiency because $ZnWO_4$ possesses a wide range of band gaps, $E_g \approx 3.2$–3.8 eV.[29–31] Moreover, these synthesis methods and conventional annealing techniques are complex, and controlling surface morphology is difficult.[32]

Conventional thermal annealing often leads to severe crystal sintering and damage to the fluorine-doped tin oxide (FTO) glass substrate. In contrast, hybrid microwave annealing enables high-temperature crystallization while effectively suppressing sintering and preserving FTO integrity, as demonstrated for Fe_2O_3, $CuFeO_2$, CuO, $ZnFe_2O_4$, and Fe_2TiO_5.[33,34] There are very few research articles available on photoelectrode preparation using an easy and inexpensive synthesis procedure for PEC water splitting applications.

In this research, we employed an α-$Fe_2O_3/ZnWO_4$ heterojunction photoanode prepared by the simple method of hydrothermal treatment with a hybrid microwave annealing approach, and the improvement of PEC water oxidation resulting from the formation of an α-$Fe_2O_3/ZnWO_4$ heterostructured photoanode was systematically studied. The recorded research shows that the α-$Fe_2O_3/ZnWO_4$ heterojunction photoanode reached maximum photocurrent density at the potential of 1.23 V (*vs.* reversible hydrogen electrode (RHE)) as compared to that of the value recorded for pure α-Fe_2O_3. The absorption of visible light of α-$Fe_2O_3/ZnWO_4$ was redshifted as compared to that of α-Fe_2O_3. This resulted in enhanced visible spectrum photon absorption, which in turn affected the increase in photocurrent density attained for the α-$Fe_2O_3/ZnWO_4$ heterojunction photoanode. Also, the formation of the α-$Fe_2O_3/ZnWO_4$ heterojunction photoanode produced an additional electric field at the *n–n* junction that was greatly decreased by the recombination of electron–hole pairs and facilitated the mobility of photoexcited charge carriers. The morphology of $ZnWO_4$ deposited on α-Fe_2O_3 to form the heterostructure was bundled nanosheets, which played an important role in increasing charge separation, and consequently increased the applied bias photon-to-current efficiency (ABPE). To the best of our knowledge, we report for the first time the synthesis of an α-$Fe_2O_3/ZnWO_4$ *n–n* heterojunction photoanode by a hybrid microwave annealing technique. The overall PEC water oxidation performance of the α-$Fe_2O_3/ZnWO_4$ *n–n* heterojunction is discussed in the results and discussion section.

2. Materials and methods

FTO (fluorine-doped tin oxide) glass substrate (resitivity approximately 7 Ω/sq) was purchased from Sigma-Aldrich. Sodium tungstate ($Na_2WO_4\cdot 2H_2O$) (assay 96%) (Nice Chemicals), iron(III) chloride ($FeCl_3\cdot 6H_2O$) (98% pure) (Sigma-Aldrich), [$Zn(NO_3)_2\cdot 2H_2O$] (assay 98%) (Molychem), ethanol AR (analytical grade) 99.9%, and hydrochloric acid were obtained for synthesis use. The complete chemical reagents were used without any further purification. Double distilled (DD) water was used as a solvent throughout the photoanode preparation.

2.1. Preparation of the α-Fe_2O_3 photoanode

A hydrothermal method was used to synthesize the α-Fe_2O_3 nanorod photoanode. The first 50 mL of a mixed solution consisting of 15% water, 35% ethanol, and 3% acetic acid with 0.1 M $FeCl_3\cdot 6H_2O$ was stirred for 30 min. The transparent solutions obtained were then transferred into a 50 mL autoclave with the FTO glass substrate (wall side facing down), and then processed with a hydrothermal treatment at 120 °C for 4 h. Then, the FeOOH films were cleaned with DD water, dried, and annealed at 700 °C for 5 min by hybrid-microwave annealing to obtain the α-Fe_2O_3 photoanode.

2.2. Preparation of the α-$Fe_2O_3/ZnWO_4$ photoanode

First, 0.25 mM of [$Zn(CH_3COO)_2\cdot 2H_2O$] was dissolved in 50 mL of DD water and then added to 0.25 mM of [$Na_2WO_4\cdot 2H_2O$] and stirred for 30 min, which yielded a transparent solution. The precursor solution was sealed in a 50 mL autoclave and maintained at 180 °C for 3 h. Finally, the obtained samples were then annealed at 550 °C for 15 min using hybrid microwave annealing and marked as α-$Fe_2O_3/ZnWO_4$. Fig. 1 shows a schematic of the formation process for the α-$Fe_2O_3/ZnWO_4$ heterojunction photoanode.

2.3 Material characterization

The morphology of the prepared photoanodes was analyzed by scanning electron microscopy (SEM) (SIGMA with Gemini Column, Carl Zeiss, USA). The elemental composition was confirmed by energy-dispersive X-ray spectrometry (EDS) using a Bruker (German) Nano XFlash Detector. The phase formation was determined by X-ray diffraction (XRD) analysis with Cu-Kα radiation, $\lambda = 1.5406$ Å, using a RigakuD/Max Ultima3i diffractometer. A UV-Vis double beam spectrometer (INFR DIGI IR-513D) was used to record light absorption between 200 and 800 nm.

2.4 PEC studies

The complete PEC measurements of the as-prepared photoanodes were examined in a standard three-electrode setup using an electrochemical workstation (BioLogic SP-150), with

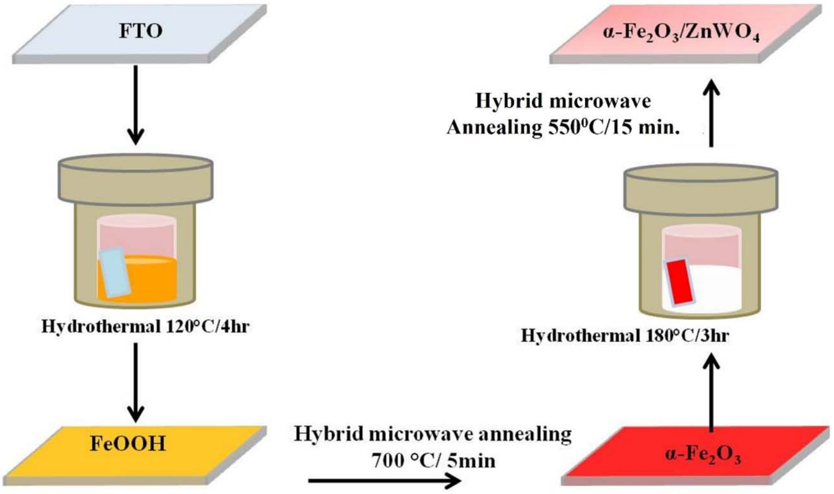

Fig. 1 A schematic diagram showing the preparation of an α-Fe_2O_3/$ZnWO_4$ heterojunction.

the α-Fe_2O_3/$ZnWO_4$ *n–n* heterojunction-based photoanode, Ag/AgCl in saturated KCl, and a platinum sheet as the working, reference, and counter electrodes, respectively. The electrolyte used was a 1 M NaOH aqueous solution. In experiments, a 150 W xenon lamp (GLORIA-X-150A) acted as the light source with an AM 1.5 G filter, with the intensity of the light at 100 mW cm^{-2}. Linear sweep voltammetry (LSV) measurements were performed at a scan rate of 10 mV s^{-1}. The chronoamperometric curves were recorded in 1 M NaOH at 1.23 V *vs.* RHE.

The electrochemical impedance spectroscopy (EIS) study was performed with a frequency range of 1–100 kHz. During the PEC measurements, the working electrode potential (*vs.* Ag/AgCl) was changed to be a scale of the RHE using the Nernst equation:[35,36]

$$E_{\mathrm{RHE}} = E_{\mathrm{Ag/AgCl}} + 0.059\ (\mathrm{pH}) + E^0{}_{\mathrm{Ag/AgCl}} \quad (1)$$

where $E_{\mathrm{Ag/AgCl}}$ indicates an experimentally measured potential against the Ag/AgCl electrode, $E^0{}_{\mathrm{Ag/AgCl}} = 0.1976$ V at 25 °C, and E_{RHE} denotes converted potential.

3. Results and discussion

Fig. 2 displays the top view FE-SEM images of the α-Fe_2O_3, $ZnWO_4$, and α-Fe_2O_3/$ZnWO_4$ photoanodes. According to the vertical (top) view FE-SEM images, the α-Fe_2O_3 appears as highly ordered and well aligned nanorods, with an average diameter of 50 ± nm after being grown on FTO film (Fig. 2a). As shown in Fig. 2b, the $ZnWO_4$ photoanode exhibits a petal-like morphology with an average length of approximately 85 ± 5 nm. The heterostructured α-Fe_2O_3/$ZnWO_4$ film (Fig. 2c) displays a mixed morphology, where $ZnWO_4$ nanoparticles are uniformly dispersed over the α-Fe_2O_3 nanorod.

This morphology suggests successful integration of both materials, which promotes the formation of heterojunctions favorable for enhanced charge separation and transport. Furthermore, the elemental composition was verified through EDS analysis (Fig. 2d), which confirmed the presence of Fe, Zn, W, and O, thus supporting the formation of the α-Fe_2O_3/$ZnWO_4$ heterostructured photoanode. The Sn signal originates from the FTO substrate. The absence of any impurity peaks indicates the high purity of the prepared heterostructure. The quantitative analysis of the composition is listed in Table 1.

To increase our understanding of the structure of α-Fe_2O_3/$ZnWO_4$, its microstructural features were examined by transmission electron microscopy (TEM), as shown in Fig. 2e and f. The low-magnification TEM image (Fig. 2e) demonstrates that the composite consists of aggregated nanostructures with intimate interfacial contact between the two semiconductors. The high-magnification TEM image (Fig. 2f) further reveals closely packed heterostructured domains at the nanoscale, indicating satisfactory dispersion of $ZnWO_4$ within the α-Fe_2O_3 matrix. Noticeably, the high-resolution transmission electron microscopy (HRTEM) image (Fig. 2g) shows well-resolved lattice fringes with interplanar spacings of 0.253 nm and 0.241 nm, which can be indexed to the (110) plane of α-Fe_2O_3 and the (021) plane of $ZnWO_4$, respectively. This clearly confirms the interface between the Fe_2O_3 nanorods and the $ZnWO_4$ heterojunction.

The corresponding SAED pattern (Fig. 2h) exhibits a series of concentric diffraction rings composed of bright spots, demonstrating the polycrystalline nature of the heterojunction. The diffraction rings can be indexed to the characteristic crystal planes of α-Fe_2O_3 and $ZnWO_4$, which is in agreement with the XRD results and further confirms the existence of both crystalline phases. Thus, it is evidenced that the formation of the α-Fe_2O_3/$ZnWO_4$ heterojunction occurred.

The XRD patterns of $ZnWO_4$, α-Fe_2O_3, and the α-Fe_2O_3/$ZnWO_4$ heterojunction are shown in Fig. 3. Fig. 3a shows the XRD patterns of FTO, and $ZnWO_4$ synthesized at 500 °C (Zn 500), 550 °C (Zn 550), and 600 °C (Zn 600). The most prominent high-intensity peaks marked with red asterisks (*) appear from the FTO substrate related to the SnO_2 characteristic peaks, while the peaks corresponding to monoclinic $ZnWO_4$ are denoted by black hearts (♥). Among the three, the $ZnWO_4$

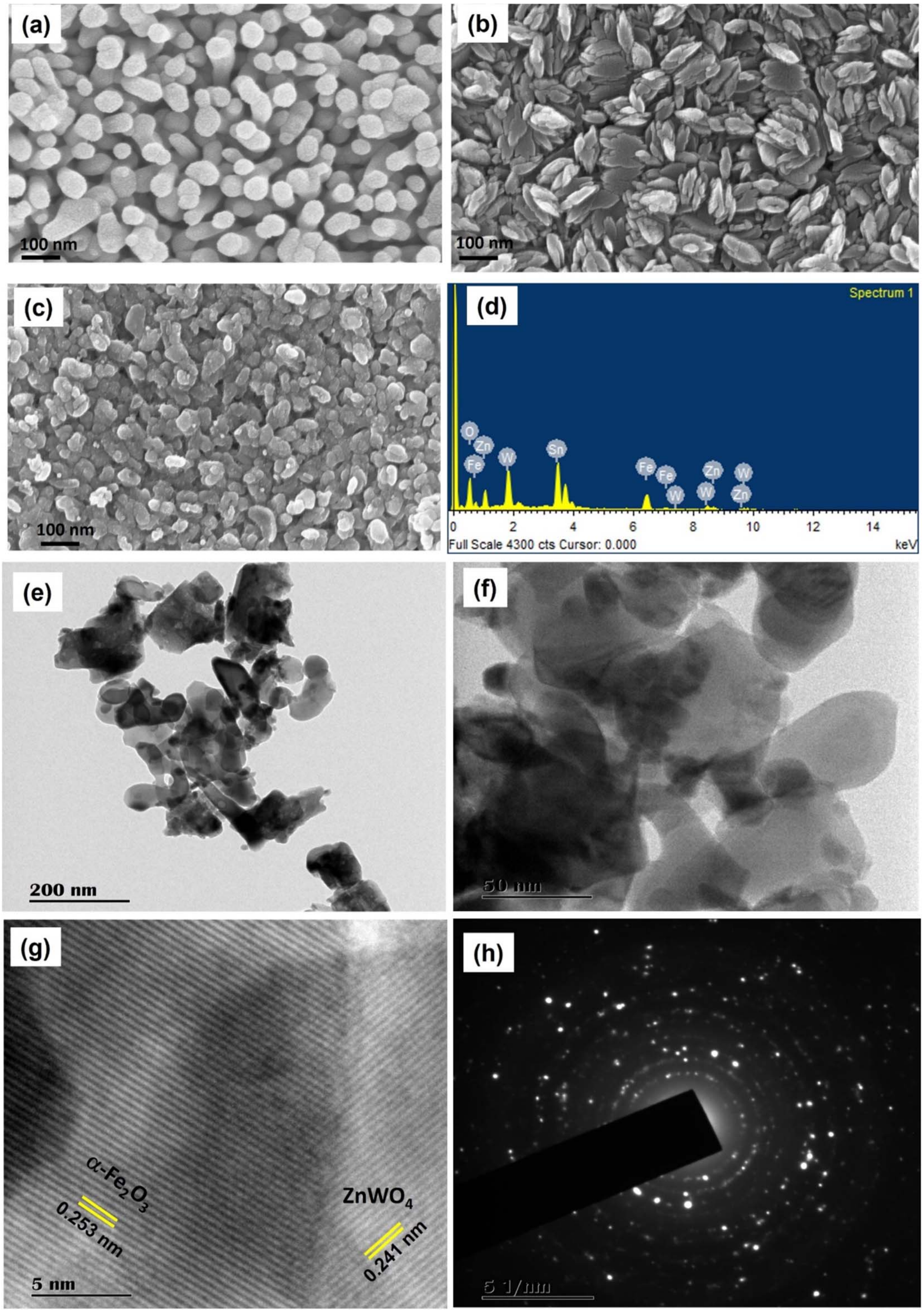

Fig. 2 FESEM images of (a) α-Fe_2O_3, (b) Zn 550, and (c) α-Fe_2O_3/$ZnWO_4$, (d) EDS spectrum and (e–h) HR-TEM images of the α-Fe_2O_3/$ZnWO_4$ heterostructure.

sample annealed at 550 °C (Zn 550) exhibits the sharpest and most intense $ZnWO_4$ diffraction peaks, indicating enhanced crystallinity compared to the 500 °C and 600 °C samples.

The lower crystallinity at 500 °C is due to incomplete phase formation, while peak broadening at 600 °C is due to thermally induced lattice strain. Hence, 550 °C is the optimal annealing temperature for $ZnWO_4$. The major diffraction peaks of $ZnWO_4$ appear at 15.43°, 18.75°, 23.9°, 31.2°, 36.2°, 47.7°, 48.7°, and 68.2°, which correspond to the (010), (100), (001), (020), (021), (030), (022), and (041) crystal planes, respectively. These peaks

Table 1 EDX elemental compositional analysis of α-Fe_2O_3/$ZnWO_4$

Composition	Sn	O	Fe	Zn	W
Weight%	33.01	34.08	10.33	3.66	18.92
Atomic%	10.11	77.40	6.72	6.72	3.74

match well with the standard data for $ZnWO_4$, confirming its formation in the monoclinic crystal system (JCPDS: 15-0774).[37]

As for α-Fe_2O_3, there are two diffraction peaks located at 35.6° and 64.2°, which correspond to the (110) and (300) planes of the rhombohedral crystal phase of α-Fe_2O_3 (JCPDS: 33-0664) (Fig. 3b).[31] In the α-Fe_2O_3/$ZnWO_4$ heterojunction, peaks for $ZnWO_4$ and α-Fe_2O_3 are observed, indicating successful formation of the heterojunction. However, the disappearance of the low-intensity $ZnWO_4$ peak at 15.43° in the heterojunction photoanode is due to the reduced crystallite size, interfacial strain, and partial peak overlap with α-Fe_2O_3, all of which suppress its detectability.

UV-visible spectroscopy was performed to understand the light-absorption mechanisms of the α-Fe_2O_3/$ZnWO_4$ heterojunction photoanode, which ranges in wavelength from 400 to 800 nm (Fig. 4a). It is clearly shown that the light absorption edge of the α-Fe_2O_3/$ZnWO_4$ photoanode significantly redshifted when compared to $ZnWO_4$ and α-Fe_2O_3, which is due to the formation of the heterojunction.[38,39] The bandgap can be estimated using a Tauc plot, which is shown in Fig. 4b. According to the Tauc result, the band gap of monoclinic $ZnWO_4$ was estimated to be 3.2 eV, while that of α-Fe_2O_3 was 2.02 eV. The α-Fe_2O_3/$ZnWO_4$ heterojunction exhibited a slightly increased band gap of 2.2 V, indicating a shift due to the interfacial electronic interaction between the two semiconductors.[29,31]

X-ray photoelectron spectroscopy (XPS) was conducted to examine the elemental composition and chemical states of the α-Fe_2O_3/$ZnWO_4$ heterojunction photoanode. The survey spectrum (Fig. 5a) confirms the presence of Fe, Zn, W, O, and Sn elements, revealing the successful composition of the heterojunction. In Fig. 5b, the high-resolution Fe 2p spectrum exhibits

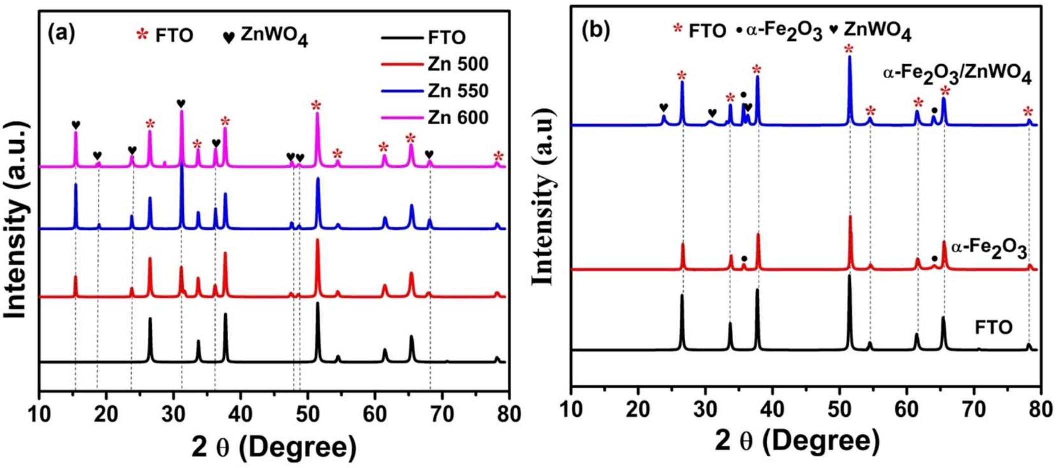

Fig. 3 XRD patterns of (a) $ZnWO_4$ annealed at different temperatures and the (b) Zn 550, α-Fe_2O_3, and α-Fe_2O_3/$ZnWO_4$ heterojunction photoanodes.

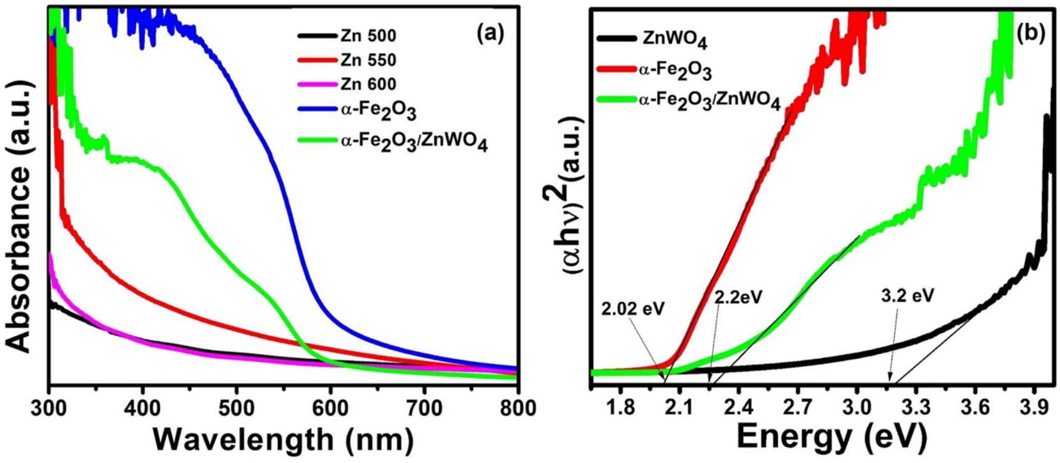

Fig. 4 (a) UV-Vis spectrum and (b) Tauc plot of the $ZnWO_4$, α-Fe_2O_3, and α-Fe_2O_3/$ZnWO_4$ heterojunction photoanodes.

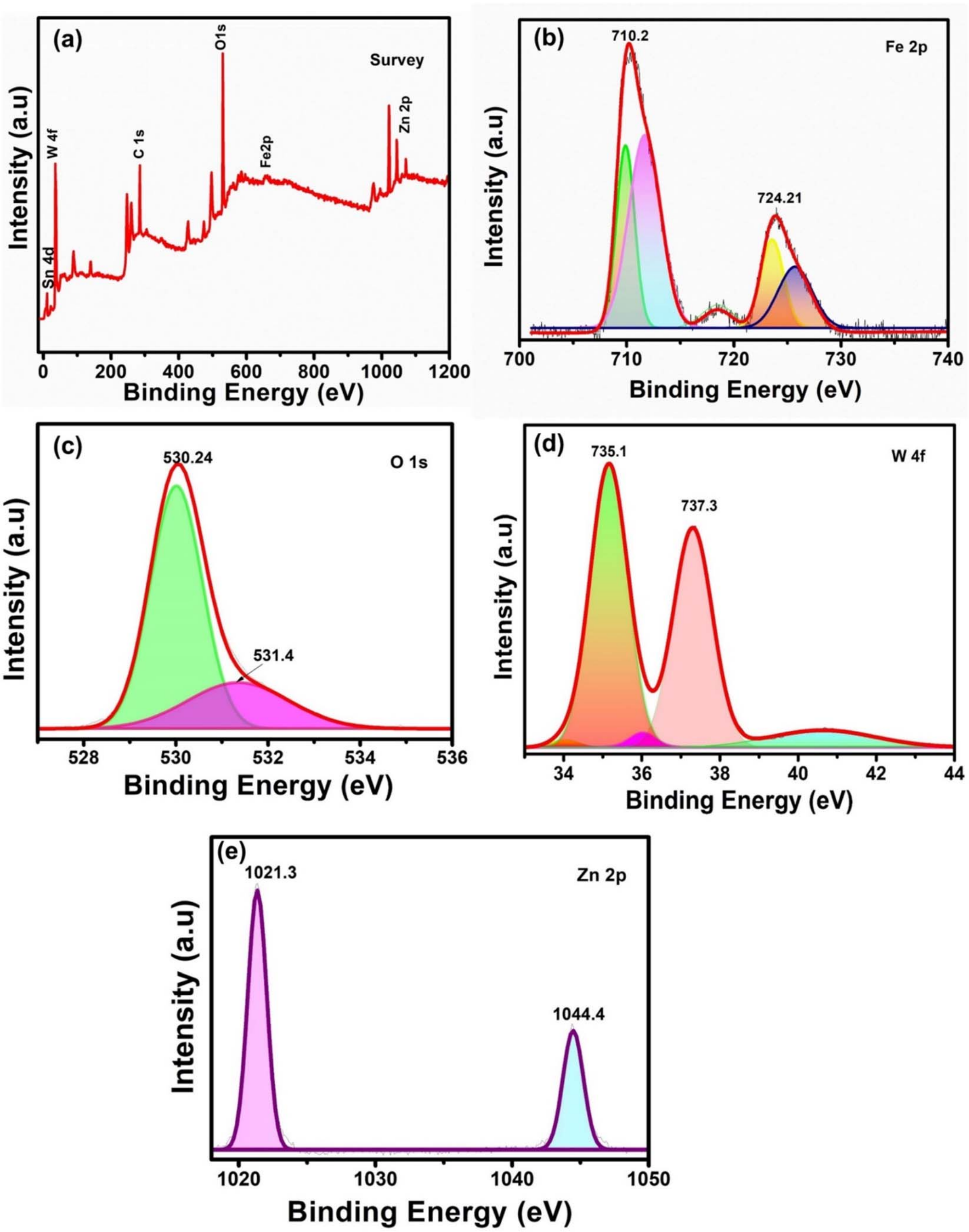

Fig. 5 XPS spectra of the α-Fe_2O_3/$ZnWO_4$ (a) survey, (b) Fe 2p, (c) O 1s, (d) Zn 2p, and (e) W 4f.

two prominent peaks corresponding to Fe $2p_{3/2}$ and Fe $2p_{1/2}$, located at 710.2 eV and 724.21 eV, respectively.

It is well known that the core-level binding energy of an element increases with an increasing valence (oxidation) state, due to the enhanced effective nuclear charge experienced by the core electrons. In the case of iron oxides, this trend is clearly reflected in the Fe 2p spectra. The Fe $2p_{3/2}$ binding energy is typically located at approximately 709 eV for Fe^{2+} species, while it shifts to higher binding energies (710–711 eV) for Fe^{3+} species. In the present α-Fe_2O_3/$ZnWO_4$ photoanode, the Fe $2p_{3/2}$ peak appears at 710.2 eV. In addition, the binding energy of a distinct shake-up satellite peak was observed at 718.6 eV, which is fully consistent with the Fe^{3+} oxidation state in the α-Fe_2O_3 phase, as previously reported.[40]

The O 1s spectrum (Fig. 5c) shows two deconvoluted peaks at 530.24 eV and 531.4 eV.[39] The lower binding energy peak was attributed to lattice oxygen (O^{2-}), while the higher binding energy peak was attributed to surface-adsorbed oxygen or hydroxyl species. Surface oxygen species are beneficial for PEC activity by favoring charge separation and surface reaction.

The W 4f spectrum (Fig. 5d) shows peaks at 35.1 eV and 37.3 eV, which were attributed to W $4f_{7/2}$ and W $4f_{5/2}$, respectively. The two peaks are associated with the photoelectrons emitted from W atoms in the W^{6+} oxidation state, which agrees with the report of $ZnWO_4$. Furthermore, there was a spin orbit separation of approximately 2.2 eV, which is consistent with W^{6+} species in $ZnWO_4$. No additional peaks corresponding to reduced tungsten species (W^{5+} or W^{4+}) were detected, suggesting that tungsten exclusively exists in the W^{6+} oxidation state. This confirms the formation of stoichiometric $ZnWO_4$ and its stable integration with α-Fe_2O_3. Fig. 5e displays the Zn 2p spectrum, which includes two peaks at 1021.3 eV and 1044.4 eV, corresponding to Zn $2p_{3/2}$ and Zn $2p_{1/2}$, respectively. The peaks indicate the 2+ oxidation state of Zn in $ZnWO_4$. The existence of a distinct Zn 2p peak also supports the successful integration of $ZnWO_4$ with α-Fe_2O_3.[41]

The PEC behavior and interfacial charge transport properties of Zn 550, α-Fe_2O_3, and their heterojunction (α-Fe_2O_3/$ZnWO_4$) were systematically evaluated, and are shown in Fig. 6. Fig. 6a shows the photocurrent density (*J*–*V*) curves for $ZnWO_4$ thin films annealed at different temperatures (500 °C, 550 °C, and 600 °C). The $ZnWO_4$ sample annealed at 550 °C exhibited the highest photocurrent density, indicating an optimal crystalline structure and enhanced photoactivity at this temperature. Fig. 6b shows the photocurrent response of pristine Zn 550, pristine α-Fe_2O_3, and their heterostructure (α-Fe_2O_3/$ZnWO_4$) under solar illumination. Among the three, the heterojunction exhibited significantly enhanced photocurrent density, reaching 0.86 mA cm^{-2} at 1.23 V *vs.* RHE, which is much higher than pristine α-Fe_2O_3 (0.29 mA cm^{-2}) or Zn 550 (0.05 mA cm^{-2}), while the corresponding photocurrent measurements recorded in the presence of H_2O_2 are provided in Fig. S1. This is due to the enhanced charge separation and decreased recombination caused by the favorable band alignment in the heterojunction.

The black solid circle shows that the dark current of α-Fe_2O_3 and α-Fe_2O_3/$ZnWO_4$ is steady and approximately zero. These indicate that the photoexcited carriers are crucial to the generation of photocurrent, and the α-Fe_2O_3/$ZnWO_4$ heterojunction obviously enhanced the photoexcited carriers, which significantly accelerated the PEC water oxidation.[42] Table S1 summarizes the α-Fe_2O_3-based heterojunction photoanodes and their corresponding PEC performance (photocurrent density at 1.23 V *vs.* RHE mA cm^{-2}). Furthermore, the efficiency of charge injection (η_{inj}) and charge separation (η_{sep}) were determined by the following formulas:[43,44]

$$\eta_{inj} = J_{H_2O}/J_{H_2O_2} \tag{2}$$

$$\eta_{sep} = J_{H_2O_2}/J_{abs} \tag{3}$$

where J_{H_2O} and H_2O_2 denote photo-water oxidation and hole scavenger, respectively.

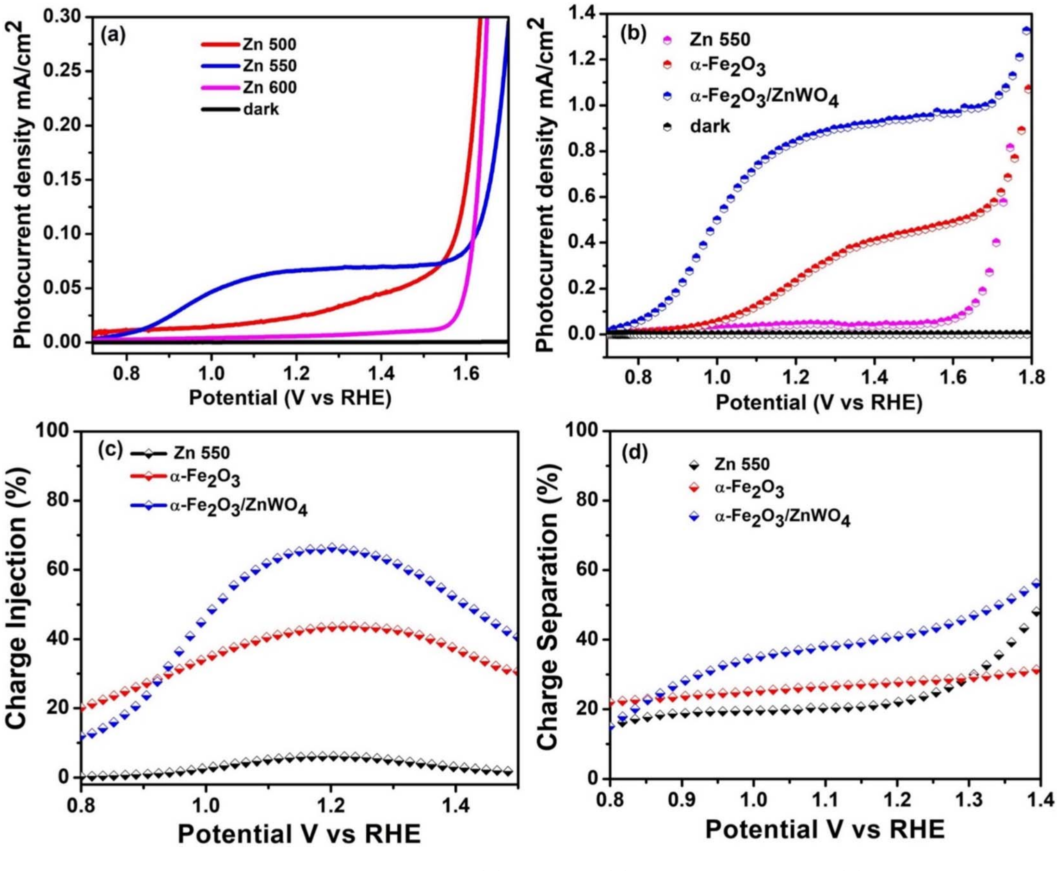

Fig. 6 (a) LSV plots of $ZnWO_4$ annealed at different temperatures. (b) LSV plots. (c) Charge injection and (d) charge separation of the Zn 550, α-Fe_2O_3, and α-Fe_2O_3/$ZnWO_4$ heterojunction photoanodes.

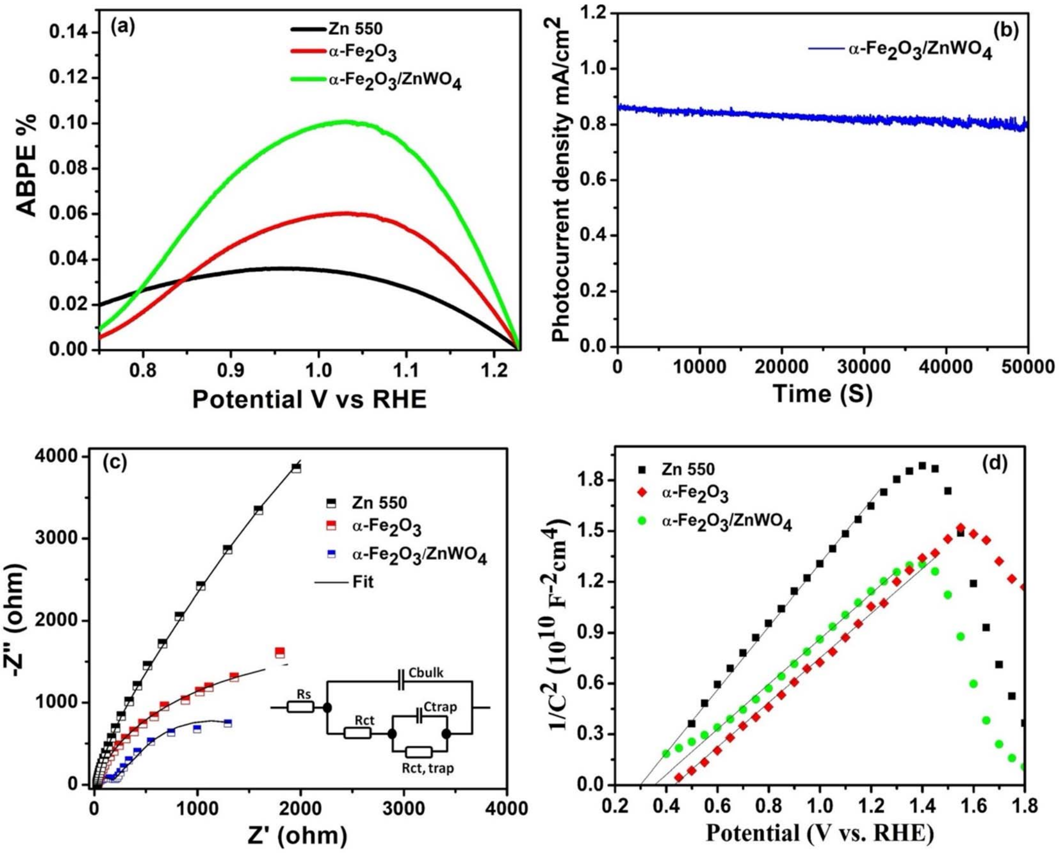

Fig. 7 (a) ABPE, (b) long-term chronoamperometry, (c) Nyquist plots, with the inset showing the equivalent circuit model, and (d) Mott–Schottky plots of the Zn 550, α-Fe_2O_3, and α-Fe_2O_3/$ZnWO_4$ photoanodes.

Fig. 6c presents the calculated charge injection efficiency as a function of applied potential. The α-Fe_2O_3/$ZnWO_4$ photoanode showed the highest injection efficiency across the entire potential range, peaking at approximately 66.16% at 1.2 V *vs.* RHE. This suggests that the heterostructure facilitates more efficient hole transfer from the semiconductor to the electrolyte compared to the individual components. Hence, the satisfactory interface injection between α-Fe_2O_3/$ZnWO_4$ and the electrolyte significantly accelerated the water oxidation process. The charge separation of α-Fe_2O_3/$ZnWO_4$ reached 42.51% at 1.23 V *vs.* RHE, which is more than that of α-Fe_2O_3 (28.30%) and Zn 550 (17.82%), as shown in Fig. 6d. These results confirm that the formation of a heterojunction effectively suppresses bulk recombination and improves carrier mobility.[45,46]

As shown in Fig. 7a, the calculated ABPE value of the α-Fe_2O_3/$ZnWO_4$ heterojunction photoanode is higher than that of the pure Zn 550 and α-Fe_2O_3 photoanodes (Table 2). The results demonstrate that the separation efficiency of the α-Fe_2O_3/$ZnWO_4$ heterojunction has significantly improved, with greater solar conversion efficiency for PEC water oxidation. The following ABPE calculations were obtained according to previously reported work.[47,48]

Table 2 Calculated η_{inj} and η_{sep} efficiencies and ABPE values

Photoanode material	η_{inj} (%)	η_{sep} (%)	ABPE (%)
Zn 550	6.45	17.82	0.033
α-Fe_2O_3	43.82	28.30	0.060
α-Fe_2O_3/$ZnWO_4$	66.13	42.51	0.10

A long-term chronoamperometry test for over 50 000 seconds for α-Fe_2O_3/$ZnWO_4$ under constant illumination shows a stable photocurrent density of approximately 0.86 mA cm^{-2}, with minimal decay (Fig. 7b). This result confirms the structural stability and resistance to photocorrosion of the heterostructure, which is critical for practical PEC applications.[49] Furthermore, the reproducible and rapid photocurrent response observed during chopped light on/off conditions demonstrates the fast charge separation and transport, as well as the satisfactory photoresponse reversibility of the α-Fe_2O_3/$ZnWO_4$ photoanode, as shown in Fig. S2.[50]

Further insight into the interfacial charge-transfer kinetics of the Zn 550, α-Fe_2O_3, and α-Fe_2O_3/$ZnWO_4$ heterojunctions was obtained by electrochemical impedance spectroscopy (EIS) measurements with fixed bias potential and frequency of 1 Hz to 100 kHz. The charge-transfer resistance and capacitance values of the Zn 550, α-Fe_2O_3, and α-Fe_2O_3/$ZnWO_4$ heterojunction photoanodes were fitted by the EIS data using an equivalent circuit model (Z fit model), as shown in Fig. 7c, and their corresponding equivalent circuit is shown in the inset in Fig. 7c.[51,52]

Table 3 The fitted EIS results

Photoanode	R_s (ohm cm^{-2})	R_2 (ohm cm^{-2})	R_{ct} (ohm cm^{-2})	C_1 (μF cm^{-2})	C_2 (μF cm^{-2})
Zn 550	36.8	860.3	645.2	0.582	4.23
α-Fe_2O_3	35.13	532.9	290.1	0.825	5.38
α-Fe_2O_3/$ZnWO_4$	30.19	143.1	52.8	3.783	15.26

Table 4 Parameters from Mott–Schottky plots for the α-Fe_2O_3 and α-Fe_2O_3/$ZnWO_4$ photoanodes

Photoanode	Donor density (cm^{-3})	Flatband potential
Zn 550	0.0067×10^9	0.30
α-Fe_2O_3	0.152×10^9	0.43
α-Fe_2O_3/$ZnWO_4$	0.147×10^{12}	0.35

In this Z fit model, R_s denotes all the series resistance in the PEC cell, including the resistance of the FTO substrate.[53] The R_{trap} denotes the charge trapping resistance in the bulk semiconductor photoelectrode, and R_{ct} represents the charge-transfer resistance across the bulk/electrolyte interface.[54] In addition, C_{bulk} and C_{trap} reflect the space-charge capacitance of the bulk and Helmholtz capacitance at the photoanode/electrolyte interface, respectively.[55] However, the fitting values of R_{trap} and R_{ct} for the α-Fe_2O_3/$ZnWO_4$ heterojunction photoanode are significantly decreased (Table 3) compared to those of the pristine α-Fe_2O_3 and $ZnWO_4$ photoanodes, which indicates that the surface trapping and transfer of photogenerated holes in the α-Fe_2O_3/$ZnWO_4$ heterojunction photoanode is much easier than that in the α-Fe_2O_3 and $ZnWO_4$ photoanodes. The EIS results clearly demonstrate the formation of the $ZnWO_4$ heterojunction on α-Fe_2O_3, which can significantly promote the surface charge transfer during the water oxidation reaction and accelerate the separation of (e^-)/(h^+).

The Mott–Schottky plots of the α-Fe_2O_3 and α-Fe_2O_3/$ZnWO_4$ heterojunction photoanodes were created to understand the semiconductor type (Fig. 7d). The carrier density and flat band potential were calculated using the Mott–Schottky equation:[56,57]

$$1/C^2 = 2/\varepsilon\ \varepsilon_0\ eN_D\ [(V{-}V_{FB}) - kT/e)] \tag{4}$$

where C denotes the specific capacitance, V denotes the applied bias potential of the α-Fe_2O_3 photoelectrode, V_{FB} denotes the flat band potential, kT/e specifies the term of temperature-dependent correction, e denotes the charge of the electron, N_D denotes the electron density, and ε, ε_0 denote the represented dielectric constant and permittivity of vacuum of α-Fe_2O_3, respectively. The positive slope of the α-Fe_2O_3 and α-Fe_2O_3/$ZnWO_4$ heterojunction photoanodes suggests that they are n-

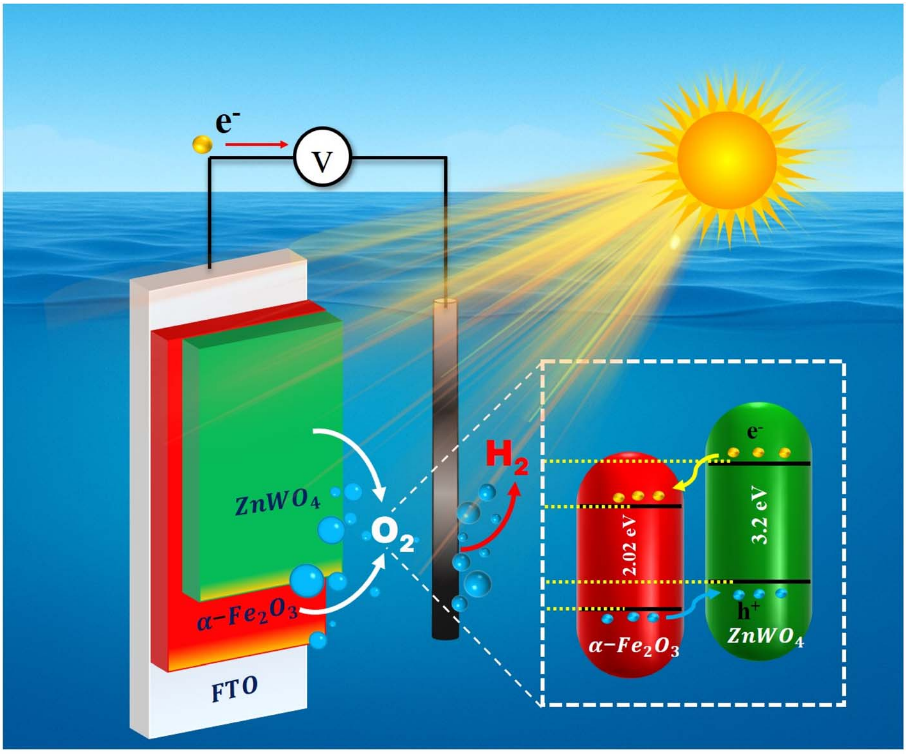

Fig. 8 Proposed mechanism of the charge transfer of an α-Fe_2O_3/$ZnWO_4$ heterojunction photoanode.

type semiconductor materials. The V_{FB} and a donor density of both photoanodes are listed in Table 4. The donor density of the α-Fe_2O_3/$ZnWO_4$ heterojunction is 0.147×10^{12}, which is much greater than that of pure Zn 550 and α-Fe_2O_3. Therefore, the staggered *n*–*n* heterojunction is beneficial for additional electronic properties in α-Fe_2O_3 films and satisfactory PEC water oxidation performance.

The proposed charge transfer and reaction mechanism of the α-Fe_2O_3/$ZnWO_4$ heterojunction photoanode under solar illumination are shown in Fig. 8. Upon light excitation, α-Fe_2O_3 and $ZnWO_4$ absorb incident photons and generate electron–hole (e^-/h^+) pairs. Because of the favorable band alignment between α-Fe_2O_3 ($E_g \approx 2.02$ eV) and $ZnWO_4$ ($E_g \approx 3.2$ eV), the photogenerated electrons in the conduction band (CB) of $ZnWO_4$ are driven toward the conduction band of α-Fe_2O_3, while the holes remain in the valence band (VB) of $ZnWO_4$. The CB and VB positions of α-Fe_2O_3 and $ZnWO_4$ were estimated based on previously reported work.[58] The CB and VB edges of α-Fe_2O_3 are located at +0.37 V and +2.39 V *vs.* NHE, respectively, with an electron affinity (χ) of approximately 5.88 eV, while $ZnWO_4$ exhibits a CB position at +0.21 V, a VB position at +3.41 V *vs.* RHE, and an electron affinity (χ) of approximately 6.31 eV.[59,60]

The accumulated holes on the valence band of $ZnWO_4$ possess sufficient oxidation potential to drive the oxygen evolution reaction (OER), leading to the generation of O_2 from water oxidation at the photoanode surface. Simultaneously, the transferred electrons in the conduction band of α-Fe_2O_3 are transported through the FTO substrate and the external circuit towards the counter electrode, where they participate in the hydrogen evolution reaction (HER) to produce H_2. Thus, the formation of the α-Fe_2O_3/$ZnWO_4$ *n*–*n* type heterojunction significantly enhanced the charge separation efficiency, accelerated the interfacial charge transfer, and improved the overall PEC water-splitting performance.

4. Conclusion

We designed an α-Fe_2O_3/$ZnWO_4$ heterojunction photoanode for PEC water splitting. The formation of a heterojunction between α-Fe_2O_3 and a $ZnWO_4$ nanostructured array significantly increased the photocurrent density by 2.2-fold. Moreover, there was a higher ABPE value (0.10%) for the α-Fe_2O_3/$ZnWO_4$ heterojunction. This could be due to the improved light absorption as well as the improved transport properties of the α-Fe_2O_3/$ZnWO_4$ heterojunction photoanode.

More specifically, the $ZnWO_4$ hole storage layer effectively reduced the transport charge resistance so that holes were stored in the $ZnWO_4$ heterojunction layer, resulting in enhanced electron–hole separation efficiency. This work demonstrates a method for fabricating highly active heterojunction photoanodes by hybrid microwave annealing that is an emerging and noticeably viable route to improve PEC performance.

Conflicts of interest

There are no conflicting interests.

Data availability

The data presented in this article are available from the corresponding author on reasonable request.

Supplementary information (SI) is available. See DOI: https://doi.org/10.1039/d5ra07601c.

Acknowledgements

This research work was supported by the Anusandhan National Research Foundation (ANRF) under the Partnerships for Accelerated Innovation and Research (PAIR) project, Government of India, sanction order ANRF/PAIR/2025/000011/PAIR-B. The authors acknowledge UGC-DAE CSR (F. No. CRS/2022–23/04/897) and DoTE (F. No. CMRG/37491/H3/2022/062) for financial support.

References

1 D. Chen, Z. Liu and S. Zhang, Enhanced PEC performance of hematite photoanode coupled with bimetallic oxyhydroxide NiFeOOH through a simple electroless method, *Appl. Catal. B Environ.*, 2020, **265**, 118580.

2 Q. Cai, Z. Liu, C. Han, Z. Tong and C. Ma, $CuInS_2$/Sb_2S_3 heterostructure modified with noble metal co-catalyst for efficient photoelectrochemical water splitting, *J. Alloys Compd.*, 2019, **795**, 319–326.

3 S. Zhang, Z. Liu, D. Chen and W. Yan, An efficient hole transfer pathway on hematite integrated by ultrathin Al_2O_3 interlayer and novel CuCoOx cocatalyst for efficient photoelectrochemical water oxidation, *Appl. Catal. B Environ.*, 2020, **277**, 119197.

4 X. Chen, M. Ruan, C. Wang, T. Zhong and Z. Liu, Phase engineering to construct In_2S_3 heterophase junctions and abundant active boundaries and surfaces for efficient Pyro-PEC performance in CdS/In_2S_3, *J. Mater. Chem. A*, 2024, **12**, 15440–15452.

5 P. J. Megía, A. J. Vizcaíno, J. A. Calles and A. Carrero, Hydrogen Production Technologies: From Fossil Fuels toward Renewable Sources. A Mini Review, *Energy Fuels*, 2021, **35**, 16403–16415.

6 K. Beasy, O. Ajulo, S. Emery, S. Lodewyckx, C. Lloyd and A. Islam, Advancing a hydrogen economy in Australia: Public perceptions and aspirations, *Int. J. Hydrogen Energy*, 2024, **55**, 199–207.

7 P. Wang, Z. Liu, C. Han, X. Ma, Z. Tong and B. Tan, Cu_2O/CuO heterojunction formed by thermal oxidation and decorated with Pt co-catalyst as an efficient photocathode for photoelectrochemical water splitting, *J. Nanoparticle Res.*, 2021, **23**, 268.

8 D. Yin, X. Ning, Q. Zhang, P. Du and X. Lu, Dual modification of $BiVO_4$ photoanode for synergistically boosting photoelectrochemical water splitting, *J. Colloid Interface Sci.*, 2023, **646**, 238–244.

9 M. Mollavali, C. Falamaki and S. Rohani, Efficient light harvesting by NiS/CdS/ZnS NPs incorporated in C, N-co-doped-TiO_2 nanotube arrays as visible-light sensitive

multilayer photoanode for solar applications, *Int. J. Hydrogen Energy*, 2018, **43**, 9259–9278.

10 J. Kegel, I. M. Povey and M. E. Pemble, Zinc oxide for solar water splitting: A brief review of the material's challenges and associated opportunities, *Nano Energy*, 2018, **54**, 409–428.

11 J. Zhang, X. Chang, C. Li, A. Li, S. Liu, T. Wang and J. Gong, WO_3 photoanodes with controllable bulk and surface oxygen vacancies for photoelectrochemical water oxidation, *J. Mater. Chem. A*, 2018, **6**, 3350–3354.

12 Y. Makimizu, N. T. Nguyen, J. Tucek, H. Ahn, J. Yoo, M. Poornajar, I. Hwang, S. Kment and P. Schmuki, Activation of α-Fe_2O_3 for Photoelectrochemical Water Splitting Strongly Enhanced by Low Temperature Annealing in Low Oxygen Containing Ambient, *Chem. Eur. J.*, 2020, **26**, 2685–2692.

13 S. S. Kalanur, I.-H. Yoo, K. Eom and H. Seo, Enhancement of photoelectrochemical water splitting response of WO_3 by Means of Bi doping, *J. Catal.*, 2018, **357**, 127–137.

14 J.-W. Lee, K.-H. Cho, J.-S. Yoon, Y.-M. Kim and Y.-M. Sung, Photoelectrochemical water splitting using one-dimensional nanostructures, *J. Mater. Chem. A*, 2021, **9**, 21576–21606.

15 Y. Li, J. Feng, H. Li, X. Wei, R. Wang and A. Zhou, Photoelectrochemical splitting of natural seawater with α-Fe_2O_3/WO_3 nanorod arrays, *Int. J. Hydrogen Energy*, 2016, **41**, 4096–4105.

16 A. Singh, R. Tejasvi, S. Karmakar and S. Basu, α-Fe_2O_3 nanorods decorated with $NiMnO_3$ co-catalyst as photoanode for enhanced oxygen evolution reaction in photoelectrochemical water splitting, *Mater. Today Commun.*, 2021, **27**, 102231.

17 X. Qi, G. She, M. Wang, L. Mu and W. Shi, Electrochemical synthesis of p-type Zn-doped α-Fe_2O_3 nanotube arrays for photoelectrochemical water splitting, *Chem. Commun.*, 2013, **49**, 5742.

18 P. Garg, L. Mohapatra, A. K. Poonia, A. K. Kushwaha, K. N. V. D. Adarsh and U. Deshpande, Single Crystalline α-Fe_2O_3 Nanosheets with Improved PEC Performance for Water Splitting, *ACS Omega*, 2023, **8**, 38607–38618.

19 N. A. Arzaee, M. F. Mohamad Noh, A. Ab Halim, M. A. F. Abdul Rahim, N. A. Mohamed, J. Safaei, A. Aadenan, S. N. Syed Nasir, A. F. Ismail and M. A. Mat Teridi, Aerosol-assisted chemical vapour deposition of α-Fe_2O_3 nanoflowers for photoelectrochemical water splitting, *Ceram. Int.*, 2019, **45**, 16797–16802.

20 A. M. Alotaibi, H. M. Alzahrani, S. M. Alosaimi, A. M. Alqahtani, M. A. Alhajji and M. J. Alotaibi, Photoelectrochemical water splitting using TiO_2/α-Fe_2O_3 heterojunction films produced by chemical vapour deposition, *RSC Adv.*, 2025, **15**, 31931–31945.

21 A. Mao, J. K. Kim, K. Shin, D. H. Wang, P. J. Yoo, G. Y. Han and J. H. Park, Hematite modified tungsten trioxide nanoparticle photoanode for solar water oxidation, *J. Power Sources*, 2012, **210**, 32–37.

22 L. Xia, J. Bai, J. Li, Q. Zeng, L. Li and B. Zhou, High-performance $BiVO_4$ photoanodes cocatalyzed with an ultrathin α-Fe_2O_3 layer for photoelectrochemical application, *Appl. Catal. B Environ.*, 2017, **204**, 127–133.

23 M. H. Sawal, A. A. Jalil, T. A. T. Abdullah, N. S. Hassan, M. B. Bahari, N. M. Izzudin, N. W. C. Jusoh, Y. Nagao, K. Aoki, M. N. Chong and S. Rajendran, n-n heterojunction CdS/FST photoanode for enhanced photoelectrochemical water splitting, *Int. J. Hydrogen Energy*, 2025, **104**, 336–343.

24 S. Bai, Q. Li, J. Han, X. Yang, X. Shu, J. Sun, L. Sun, R. Luo, D. Li and A. Chen, Photoanode of LDH catalyst decorated semiconductor heterojunction of $BiVO_4$/CdS to enhance PEC water splitting efficiency, *Int. J. Hydrogen Energy*, 2019, **44**, 24642–24652.

25 S. Bai, X. Yang, C. Liu, X. Xiang, R. Luo, J. He and A. Chen, An Integrating Photoanode of WO_3/Fe_2O_3 Heterojunction Decorated with NiFe-LDH to Improve PEC Water Splitting Efficiency, *ACS Sustain. Chem. Eng.*, 2018, **6**, 12906–12913.

26 S. Bai, Y. Fang, Y. Zhao, Y. Feng, R. Luo, D. Li and A. Chen, Bi nanoparticles modified the $WO_3/ZnWO_4$ heterojunction for photoelectrochemical water splitting, *J. Colloid Interface Sci.*, 2023, **646**, 745–752.

27 Y. Cui, L. Pan, Y. Chen, N. Afzal, S. Ullah, D. Liu, L. Wang, X. Zhang and J.-J. Zou, Defected $ZnWO_4$-decorated WO_3 nanorod arrays for efficient photoelectrochemical water splitting, *RSC Adv.*, 2019, **9**, 5492–5500.

28 S. Sadhasivam and T. H. Oh, Dual Discrete $ZnWO_4$/CdS, CdS/SnS_2 interface of heterostructure photoanode establishing the bias free carrier separation for solar driven water splitting, *Mater. Chem. Phys.*, 2025, **333**, 130331.

29 H. Liu, J. Huang, J. Chen, J. Zhong, J. Li and R. Duan, Preparation and characterization of novel $Ag/Ag_2WO_4/ZnWO_4$ heterojunctions with significantly enhanced sunlight-driven photocatalytic performance, *Solid State Sci.*, 2019, **95**, 105923.

30 U. K. Ghorui, P. Mondal, J. Satra, B. Adhikary and A. Mondal, In situ metallic copper incorporation into novel g-$C_3N_4/ZnWO_4$ nanocomposite semiconductor for efficient thin film solar cell application, *Mater. Sci. Semicond. Process.*, 2022, **143**, 106559.

31 M. Yin, Y. Wang and S. Liu, Synthesis of Fe_2O_3–$ZnWO_4$ nanocomposites and their enhanced acetone sensing performance, *J. Alloys Compd.*, 2020, **831**, 154713.

32 M. A. Mahadik, H. H. Lee, W.-S. Chae, M. Cho and J. S. Jang, Energy-efficient photoelectrochemical water splitting and degradation of organic dyes over microwave-assisted WO_3 nanosheets/W foil with rapid charge transport, *Sol. Energy Mater. Sol. Cells*, 2022, **246**, 111939.

33 J. H. Kim, Y. H. Jo, J. H. Kim and J. S. Lee, Ultrafast fabrication of highly active $BiVO_4$ photoanodes by hybrid microwave annealing for unbiased solar water splitting, *Nanoscale*, 2016, **8**, 17623–17631.

34 J. H. Kim, Y. J. Jang, S. H. Choi, B. J. Lee, M. H. Lee and J. S. Lee, Hybrid Microwave Annealing for Fabrication of More Efficient Semiconductor Photoanodes for Solar Water Splitting, *ACS Sustain. Chem. Eng.*, 2019, **7**, 944–949.

35 M. Mojaddami and A. Simchi, First demonstration of photoelectrochemical water splitting by commercial W–Cu powder metallurgy parts converted to highly porous 3D

WO_3/W skeletons, *Int. J. Hydrogen Energy*, 2020, **45**, 6369–6379.

36 S. Seenivasan, H. Moon and D. H. Kim, Multilayer Strategy for Photoelectrochemical Hydrogen Generation: New Electrode Architecture that Alleviates Multiple Bottlenecks, *Nano-Micro Lett.*, 2022, **14**, 1–18.

37 M. I. Osotsi, D. K. Macharia, B. Zhu, Z. Wang, X. Shen, Z. Liu, L. Zhang and Z. Chen, Synthesis of $ZnWO_4$−x nanorods with oxygen vacancy for efficient photocatalytic degradation of tetracycline, *Prog. Nat. Sci.:Mater. Int.*, 2018, **28**, 408–415.

38 K. C. Leonard, K. M. Nam, H. C. Lee, S. H. Kang, H. S. Park and A. J. Bard, $ZnWO_4/WO_3$ composite for improving photoelectrochemical water oxidation, *J. Phys. Chem. C*, 2013, **117**, 15901–15910.

39 S. Bai, Y. Fang, Y. Zhao, Y. Feng, R. Luo, D. Li and A. Chen, Bi nanoparticles modified the $WO_3/ZnWO_4$ heterojunction for photoelectrochemical water splitting, *J. Colloid Interface Sci.*, 2023, **646**, 745–752.

40 W. Ma, X. Wu, K. Huang, M. Wang, R. Fu, H. Chen and S. Feng, A Co(OH)x nanolayer integrated planar WO_3/Fe_2O_3 photoanode for efficient photoelectrochemical water splitting, *Sustain. Energy Fuels*, 2019, **3**, 2135–2141.

41 L. Tian, Y. Rui, K. Sun, W. Cui and W. An, Surface decoration of $ZnWO_4$ nanorods with cu_2O nanoparticles to build heterostructure with enhanced photocatalysis, *Nanomaterials*, 2018, **8**(1), 33.

42 A. Memar, C. M. Phan and M. O. Tade, Photocatalytic activity of WO_3/Fe_2O_3 nanocomposite photoanode, *Int. J. Hydrogen Energy*, 2015, **40**, 8642–8649.

43 A. Polo, C. Nomellini, I. Grigioni, M. V. Dozzi and E. Selli, Effective Visible Light Exploitation by Copper Molybdo-tungstate Photoanodes, *ACS Appl. Energy Mater.*, 2020, **3**, 6956–6964.

44 Z. Wang, X. Zong, Y. Gao, J. Han, Z. Xu, Z. Li, C. Ding, S. Wang and C. Li, Promoting Charge Separation and Injection by Optimizing the Interfaces of GaN:ZnO Photoanode for Efficient Solar Water Oxidation, *ACS Appl. Mater. Interfaces*, 2017, **9**, 30696–30702.

45 V. S. Kumbhar, H. Lee, J. Lee and K. Lee, Interfacial growth of the optimal $BiVO_4$ nanoparticles onto self-assembled WO_3 nanoplates for efficient photoelectrochemical water splitting, *J. Colloid Interface Sci.*, 2019, **557**, 478–487.

46 H. Dotan, K. Sivula, M. Grätzel, A. Rothschild and S. C. Warren, Probing the photoelectrochemical properties of hematite (α-Fe_2O_3) electrodes using hydrogen peroxide as a hole scavenger, *Energy Environ. Sci.*, 2011, **4**, 958–964.

47 Y. Gao, X. Li, J. Hu, W. Fan, F. Wang, D. Xu, J. Ding, H. Bai and W. Shi, Ag-Pi/$BiVO_4$ heterojunction with efficient interface carrier transport for photoelectrochemical water splitting, *J. Colloid Interface Sci.*, 2020, **579**, 619–627.

48 P. Yue, H. She, L. Zhang, B. Niu, R. Lian, J. Huang, L. Wang and Q. Wang, Super-hydrophilic CoAl-LDH on $BiVO_4$ for enhanced photoelectrochemical water oxidation activity, *Appl. Catal. B Environ.*, 2021, **286**, 119875.

49 Y. Wang, L. Cai, Y. Li, Y. Tang and C. Xie, Structural and photoelectrocatalytic characteristic of $ZnO/ZnWO_4/WO_3$ nanocomposites with double heterojunctions, *Physica E: Low Dimens. Syst. Nanostruct.*, 2010, **43**, 503–509.

50 P. S. Bassi, R. P. Antony, P. P. Boix, Y. Fang, J. Barber and L. H. Wong, Crystalline Fe_2O_3/Fe_2TiO_5 heterojunction nanorods with efficient charge separation and hole injection as photoanode for solar water oxidation, *Nano Energy*, 2016, **22**, 310–318.

51 H. Han, F. Riboni, F. Karlicky, S. Kment, A. Goswami, P. Sudhagar, J. Yoo, L. Wang, O. Tomanec, M. Petr, O. Haderka, C. Terashima, A. Fujishima, P. Schmuki and R. Zboril, α-Fe_2O_3/TiO_2 3D hierarchical nanostructures for enhanced photoelectrochemical water splitting, *Nanoscale*, 2017, **9**, 134–142.

52 S. Wannapop and A. Somdee, Effect of citric acid on the synthesis of $ZnWO_4$/ZnO nanorods for photoelectrochemical water splitting, *Inorg. Chem. Commun.*, 2020, **115**, 107857.

53 S. K. Jang, S. H. Jeong, A. Hong and W. Y. Sohn, Mitigation of the Anodic Shift of the Onset Potential in a TiO_2/α-Fe_2O_3 Photoanode by Inserting a Nickel Ferrite ($NiFe_2O_4$) Blocking Layer, *ACS Omega*, 2025, **10**, 57407–57417.

54 W. Zha, Q. Ruan, L. Kong, X. Xi, M. A. Turgunov, W. Zhang, K. Chang and Z. Sun, A suspension-mimicking hydrogel-based n-type polymer photocathode for solar-driven water splitting, *Cell Rep. Phys. Sci.*, 2022, **3**, 100863.

55 M. Serhan, M. Sprowls, D. Jackemeyer, M. Long, I. D. Perez, W. Maret, N. Tao and E. Forzani, Total iron measurement in human serum with a smartphone, AIChE Annu. Meet. Conf. Proc.

56 S. Kumar, S. Ahirwar and A. K. Satpati, Insight into the PEC and interfacial charge transfer kinetics at the Mo doped $BiVO_4$ photoanodes, *RSC Adv.*, 2019, **9**, 41368–41382.

57 K. Sivula, Mott–Schottky Analysis of Photoelectrodes: Sanity Checks Are Needed, *ACS Energy Lett.*, 2021, **6**, 2549–2551.

58 T. Zhu, L. Huang, Y. Song, Z. Chen, H. Ji, Y. Li, Y. Xu, Q. Zhang, H. Xu and H. Li, Modification of Ag_3VO_4 with graphene-like MoS_2 for enhanced visible-light photocatalytic property and stability, *New J. Chem.*, 2016, **40**, 2168–2177.

59 E. C. Pastrana, S. J. Loarte, C. D. Gonzales-Lorenzo, R. Y. P. Alta and H. A. Alarcón, Fabrication and characterization of copper (II) oxide/iron (III) oxide thin film heterostructures for trace arsenic (III) removal in water, *Thin Solid Films*, 2021, **717**, 138440.

60 Y. Wu, J. Zhang, B. Long and H. Zhang, The stability and electronic and photocatalytic properties of the $ZnWO_4$ (010) surface determined from first-principles and thermodynamic calculations, *RSC Adv.*, 2021, **11**, 23477–23490.